JOM, Vol. 75, No. 10, 2023
https://doi.org/10.1007/s11837-023-06044-6

A Novel Approach for Enhanced Mechanical Properties in Solid-State Additive Manufacturing by Additive Friction Stir Deposition Using Thermally Stable Al-Ce-Mg Alloy

ANURAG GUMASTE,[1,2] ABHIJEET DHAL,[1,2] PRIYANSHI AGRAWAL,[1,2,5] RAVI SANKAR HARIDAS,[2,3] VIJAY K. VASUDEVAN,[1] DAVID WEISS,[4] and RAJIV S. MISHRA [1,2,6]

1.—Department of Materials Science and Engineering, University of North Texas, Denton, TX 76207, USA. 2.—Center for Friction Stir Processing, University of North Texas, Denton, TX 76207, USA. 3.—Department of Mechanical Engineering, University of North Texas, Denton, TX 76207, USA. 4.—Loukus Technologies, Inc, 58390 Centennial #6 Rd, Calumet, MI 49913, USA. 5.—*Present address:* Materials Science and Technology Division, Oak Ridge National Laboratory, Oak Ridge, TN 37831, USA. 6.—e-mail: Rajiv.Mishra@unt.edu

An innovative approach to build a high-performance, thermally stable Al-8Ce-10Mg (wt.%) alloy via friction-stir based solid-state additive manufacturing, called additive friction stir deposition, has been demonstrated in this study. The deposited material displayed 22% higher yield strength and 181% improvement in ductility as compared to the base material. The deposit also exhibited excellent tensile properties at elevated temperatures. The improved performance has been attributed to multiple strengthening mechanisms active in the built component. Al-Ce particle fragmentation, grain refinement, and retention of Mg in solid solution during the process synergistically resulted in the improved mechanical performance. The fragmentation of $Al_{11}Ce_3$ particles occurred due to intense frictional heating and shearing during the process. Scanning electron microscopy, nanoindentation, tensile testing, differential scanning calorimetry, and X-ray diffraction analysis were used to establish process–structure–property correlations at multiple length scales.

INTRODUCTION

Additive manufacturing (AM) has gained research thrust in the quest to achieve sustainable manufacturing. Conventional fusion-based metal AM processes, such as powder bed fusion and directed energy deposition, have been hot topics of research in recent years.[1] These processes are advantageous in the production of functionally- and geometrically-sophisticated parts. However, the conventional fusion-based AM processes face challenges, like low rate of manufacturing, high cost of production, intricacies of process control for defect elimination, stringent quality regulations on (powder) raw material, large thermal gradients that lead to anisotropic properties, and residual stresses.[2]

A relatively new solid-state process called additive friction stir deposition (AFSD), a promising development in the AM domain, is less complex from the process control standpoint.[3] Process variables, such as tool rotation rate (ω), tool traverse speed (V), and material feed rate (F), provide a larger operating window to produce defect-free components compared to conventional fusion AM methods, whose optimum operating range is confined by lack of fusion and keyhole porosity. Moreover, the components obtained exhibit isotropic properties and possess refined equiaxed grains. The wrought microstructure of the deposit obtained by AFSD results in enhanced properties, compared to the solidification-induced microstructure in conventional fusion-based AM material. Being a high throughput process to produce bulk components, AFSD is rapidly growing as a promising solid-state AM technique. Despite numerous advantages of

(Received April 1, 2023; accepted July 24, 2023; published online August 24, 2023)

AFSD such as energy efficiency, near defect-free build capability, high scalability, wrought microstructural outcome, minimal distortion, and favorable residual stresses, tailoring the appropriate alloy composition for AFSD remains a key research gap.[4] Currently, the AFSD process is limited to commercially available alloys, and applying novel alloys to enhance material performance through AFSD requires a deeper understanding of the process variability's impact on microstructure and mechanical properties.[5] A smart alloy design approach, coupled with advanced manufacturing process, yields exceptional structural performance. Alloy chemistry can be varied in terms of elements for solutes/particles, engineering stacking fault energy, solutes for texture, and/or thermally resistant particles.[4]

Commercial heat-treatable aluminum alloys, which derive strength from metastable nanoscale precipitates, are used widely in the automobile and aerospace industries because of their high specific strength. These materials degrade in strength on friction-stir based processing as a result of dissolution of the strengthening precipitates at high process temperatures.[6] Post-process heat treatment being essential to regain strength in such situations increases the manufacturing cost and lead time.[7] Also, components manufactured using conventional Al alloys by AFSD fail to serve at elevated service temperatures due to rapid coarsening of the microstructure, promotion of grain boundary sliding, and dissolution of strengthening precipitates.[8]

Addition of rare earth (RE) elements, which are expensive, in non-ferrous alloys is of increasing interest to researchers in efforts to obtain improved material properties, such as strength, ductility, thermal stability, oxidation resistance, creep strength, age hardenability, lower anisotropy, refined microstructure, and corrosion resistance, combined with superior performance at elevated temperatures.[9,10] Cerium (Ce) is the most abundant and commonly used RE element. Al-Ce alloys have been of interest for relevant high-temperature applications, such as powertrain and engine components (like engine head and turbocharger) for the automotive and aerospace industries.[11] The Al-Ce (4–13 wt.%) cast alloys exhibit good mechanical properties.[12] Ce being the least expensive RE element, ternary alloy systems with small amounts of Ce, such as Al-Ce-Ni and Al-Cu-Ce, have been explored for improved properties at reduced cost.[13]

Al-Mg binary alloy systems are an attractive combination due to their low density and solid-solution strengthening provided by Mg. However, they depreciate in mechanical performance at elevated temperatures.[14] A novel ternary Al-8Ce-10Mg alloy has been chosen to demonstrate the synergistic effects of material–process combination to improve mechanical properties. Large differences in the coefficient of thermal expansion (CTE) between Al and Ce leads to microcracking of primary $Al_{11}Ce_3$ in the cast condition, thereby reducing ductility.[15] Choosing the eutectic composition of 10% Ce mitigates this challenge and demonstrates better ductility. Limited Ce solubility in Al-Mg leads to the formation of thermally stable intermetallic phases, which aid in improving high-temperature strength.[16] Al-16%Ce led to the formation of blocky $Al_{11}Ce_3$ intermetallics, and varying the alloying content changed the morphology of the intermetallic phase.[15] Mg/Ce ratio can be optimized to fine-tune recrystallization in the alloy. With good castability, Al-Ce-Mg alloy systems potentially lead to a new class of thermally-resistant Al alloys that have recently been explored in fusion-based AM. The Al-8Ce-10Mg alloy, printed using selective laser melting, showed nanoscale dispersion of insoluble intermetallic particles and resistance to coarsening up to 400°C.[10] The composite strengthening offered by the particles aided in improved mechanical properties. Laser AM of the Al-12Ce alloy confirmed that the melt pool transitioned from a eutectic structure at the pool boundary to a dendritic/cellular structure near the pool center.[17] Such inhomogeneity in the material can be detrimental to its mechanical properties.

Exploring a solid-state-based AM route for processing Al-Ce alloys could be an opportunity to obtain a new class of high-strength, thermally stable Al alloys in the as-deposited condition. This study has attempted maximizing the material performance by process-specific alloy selection for AFSD. Figure 1 shows the mechanical property comparison of typical AFSDed non-ferrous alloys. The current work has harnessed the synergistic advantages of AFSD process attributes and alloy characteristics to enhance the mechanical performance in the as-deposited state. It has also investigated the mechanisms that lead to the superior

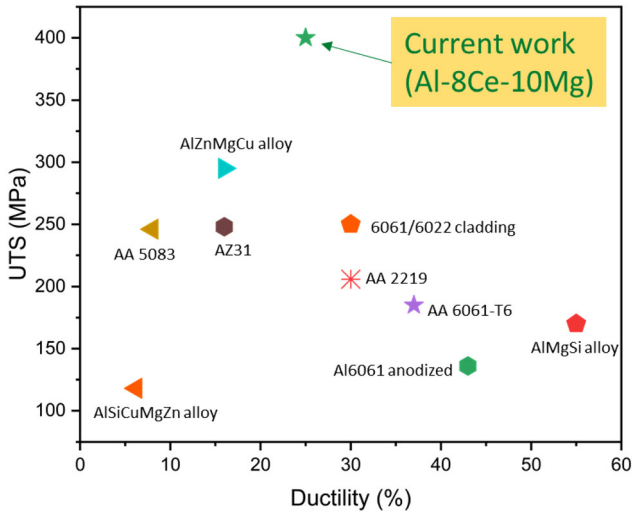

Fig. 1. Comparison of UTS versus ductility for typical light structural alloys deposited by AFSD. The data used in this figure are a generic representation of literature information.[8,18–25]

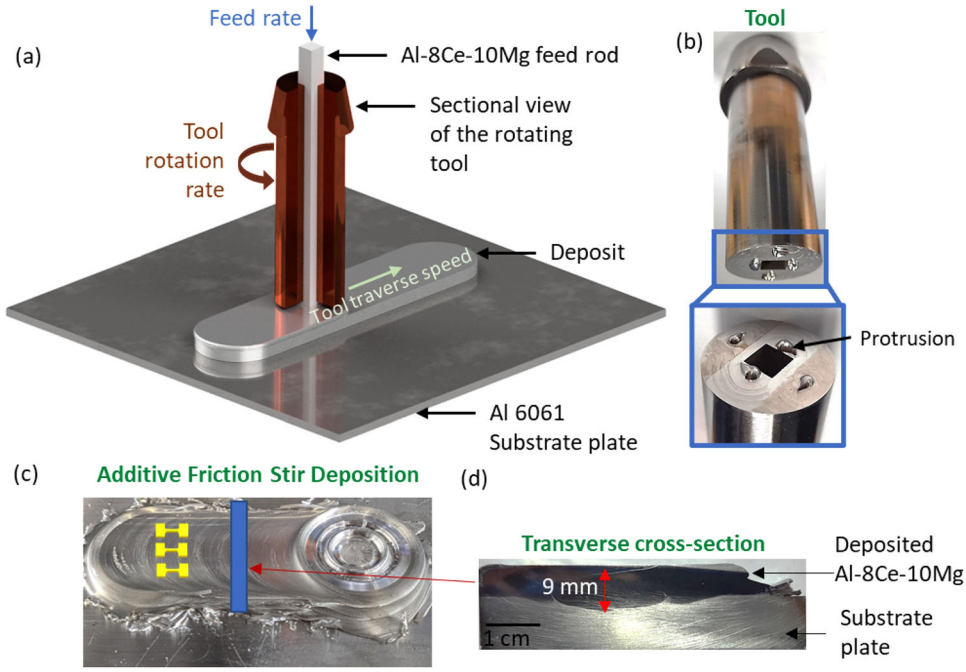

Fig. 2. (a) Schematic of AFSD process, (b) special protruded tool used for deposition, (c) image of AFSD Al-8Ce-10Mg with representative sample sectioning location, and (d) image of the transverse cross-section of the sample characterized in this work.

performance of the Al-8Ce-10Mg alloy processed via AFSD. For this, a multiscale process–structure–property correlative study was conducted.

METHOD AND MATERIALS

AFSD of Al-8Ce-10Mg was performed using a MELD B8 machine (Meld Manufacturing). A schematic of the AFSD process is shown in Fig. 2a. During AFSD, the feedstock is fed through a hollow rotating tool. Under high forge loads, the feedstock plasticizes and extrudes beneath the tool to deposit multiple layers. The tool is traversed along different axes to deposit a 3D component. A tool made of H13 steel having a diameter of 38.1 mm with four teardrop-shaped protrusions of 2 mm height was used for the deposition (Fig. 2b). The as-received Al-8Ce-10Mg base material (BM; by Eck Industries) was in the form of extruded bars, which were subsequently sectioned into 150-mm-long square feedstock rods of 9.5 mm × 9.5 mm using KENT electrical discharge machining. Graphite spray was used to lubricate the feedstock rods during AFSD. Three such rods yielded a deposit of seven layers measuring 76.2 mm in length and 1 mm thick, deposited at optimized parameters of 250 rpm tool rotation rate, 254 mm/min tool traverse speed, and 152.4 mm/min feed rate. Al 6061 substrate plate (300 mm length × 300 mm width × 10 mm thick) was used for deposition.

Figure 2c shows the image of AFSDed Al-8Ce-10Mg. The BM and AFSD materials were sectioned and polished up to 0.02 μm for metallographic analysis. A Quanta scanning electron microscope (SEM; FEI) operating at 20 kV was used for basic microstructural characterization and electron dispersive spectroscopy (EDS). Electron backscatter diffraction (EBSD) characterization of the microstructure was performed using a Nova NanoSEM 230 (FEI) equipped with a Hikari Super EBSD detector at an operating voltage of 20 kV. TEAM^{TM} and TSL OIM Analysis^{TM} 8 softwares were used for EBSD data acquisition and analysis, respectively. Rectangular dog-bone-shaped mini-tensile samples of 5 mm gage length, 1.25 mm width, and 1 mm thickness, as shown in Fig. 2c, were sectioned along the traverse direction using a Tormach PCNC 440 milling machine. Tensile tests were performed at room temperature (RT) on a custom-made mini-tensile tester at an engineering strain rate of 10^{-3} s^{-1}. To ensure statistical precision, three samples were tested for each condition. Micrographs of the fractured surfaces were also captured using SEM. Hardness line scans were performed along the build direction using a Vickers microhardness tester (VH3300; Wilson) at a load of 0.5 Kgf. Nanoindentation tests on the samples were performed with a FemtoTools FT-NMT04 nanoindenter using a Berkovich indenter in displacement-control mode with a limiting depth of 0.2 μm. The loading and unloading rates were 0.075 μN/s and 1.5 μN/s, respectively. The nanoindentation grid consisted of 250 indents covering a wide range of particle heterogeneity in both base and processed conditions. Continuous stiffness measurement was employed, and an inter-indent spacing of 3 μm was maintained during nanoindentation.

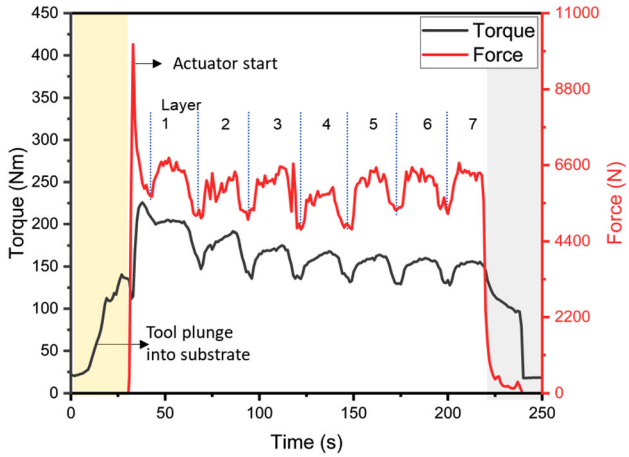

Fig. 3. Torque/Force–Time plots for the Al-8Ce-10Mg deposit.

Microstructure and phase analysis of BM and AFSD material was performed by X-ray diffraction (XRD) using CuKα (λ = 0.154 nm) radiation in Ultima III diffractometer (Rigaku) operated at 40 kV and 44 mA. Differential scanning calorimetry (DSC) was performed using a 204F1 Phoenix® system (Netzsch). The tests were accomplished over a temperature range of 20–500°C at a rate of 20°C min^{-1}. ThermoCalc 2023a was used to study the equilibrium phase evolution in the alloy with increasing temperature from RT to melting point. TCAL8 Al-Alloys v8.2 and MOBAL7 (Al-alloys Mobility version 7.0) databases were used for this computation.

RESULTS AND DISCUSSION

AFSD Process Dynamics

Figure 3 shows the temporal variation in spindle torque and actuator force during the deposition of seven layers. Torque initially increases steadily due to tool protrusions engaging with the substrate plate. Actuator feed was started on sufficient heat generation when the tool was in complete contact with the substrate. The actuator force increased sharply on starting the feed and then plummeted, indicating sufficient plasticizing of the feed rod due to frictional heat generated on interaction with the substrate plate. Each hump denotes the deposition of one layer (marked 1–7 in Fig. 3). Steady-state force values were approximately constant for all seven layers. The steady decrease in torque values for subsequent layers can be attributed to heat accumulation occurring in the deposit as build height increases. Average steady-state forge force during deposit was approximately 6247.5 N, while average steady-state torque was approximately 173.4 Nm. Conceptual model derived for the AFSD process shows that power and specific energy consumption are dependent on spindle torque, and in turn influence heat input to the system.[4] Pew et al.[26] developed a torque-based heat input model for friction stir welding using an empirical relationship:

$$\text{Weld power} = \frac{2\pi N\tau}{60}, \quad \text{and} \tag{1}$$

$$\text{Heat input(HI)} = \frac{2\pi N\tau}{60v}, \tag{2}$$

where N is the tool rotation rate in rpm, τ is torque in Nm, and v is the tool traverse speed in m/s. Weld power and HI are in watts and joules, respectively. Using these empirical relationships, the average power consumed during steady-state AFSD was calculated as 4.53 kW and HI as 1071.8 kJ/m. Arbegast and Hartley correlated the maximum temperature during friction stir welding with a pseudo-heat index function (ω^2/v), which is also applicable to AFSD.[27,28] Maximum welding temperature T (in °C) is given by:

$$\frac{T}{T_m} = K\left(\frac{\omega^2}{v \times 10^4}\right)^{\alpha}, \tag{3}$$

where T_m (in °C) is the alloy melting point, ω is the tool rotation rate, exponent α varies from 0.04 to 0.06, and constant K varies from 0.65 to 0.75. Using Eq. 3 and the melting point of Al-8Ce-10Mg alloy being approximately 590°C, the peak deposition temperature can be approximated to be 421°C, using α = 0.05 and K = 0.7.

Particle Fragmentation During AFSD

Figure 4a shows SEM micrograph of the BM, which possesses a combination of large and small intermetallic $Al_{11}Ce_3$ particles ranging from 0.4 μm to 130 μm. These particles are aligned along the extrusion direction in the Al-Mg matrix. Figure 4b confirms that $Al_{11}Ce_3$ intermetallics were broken down to smaller sizes and were evenly distributed throughout the matrix during AFSD. No visible evidence of process-related defects in the deposit demonstrates that AFSD is an effective route to develop near-defect-free Al-Ce-Mg alloy components. Figure 4c presents a SEM micrograph montage of the top six layers. The deposit shows that larger chunks of $Al_{11}Ce_3$ present in the BM were broken down and distributed homogeneously throughout the matrix after AFSD. Additionally, the protrusions on the tool shoulder break the interface layer during subsequent deposits, resulting in a sound interlayer bonding. The micrographs in Fig. 4a and b were analyzed using image processing software (ImageJ) to quantify the particle size distribution in BM and AFSD samples, and the histogram is displayed in Fig. 4d. Particle size was measured in terms of equivalent diameter. A broad distribution in the size of intermetallic particles can be noted in the BM compared to the AFSD sample. The BM had particles ranging from

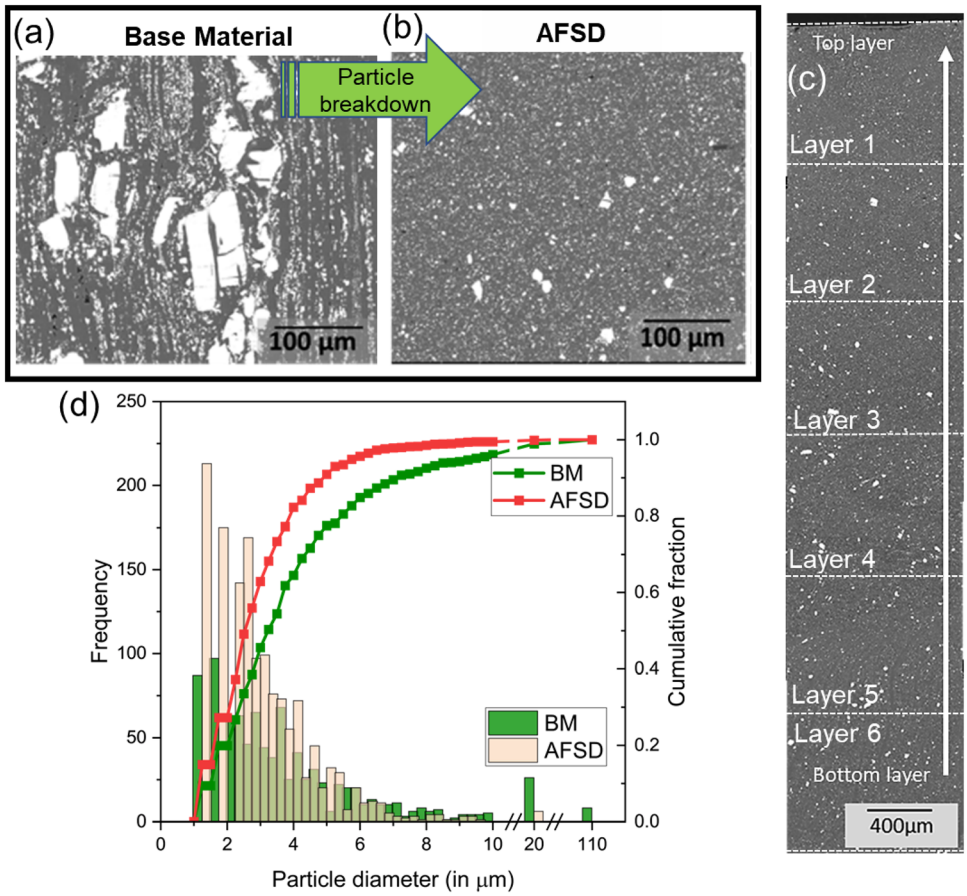

Fig. 4. Particle fragmentation after AFSD: (a) SEM micrographs of BM and (b) AFSD, (c) montage of SEM micrographs captured along the build direction, and (d) particle size analysis of BM and AFSD.

submicron to as large as 110 μm. Note that 5% of the particles were greater than 10 μm in size, 75% were less than 5 μm, and 20% were between 5 μm and 10 μm. In contrast, after AFSD, 75% of the particles were below 3.5 μm, 95% were below 5 μm, and only 0.5% were greater than 10 μm. No particles greater than 20 μm in the AFSD sample indicates that, due to intense shear deformation occurring during the process, the particles were broken down to smaller sizes and distributed uniformly throughout the matrix.

Figure 5 captures the mechanism of particle breakdown that occurs during AFSD. The intermetallic particles undergo intense cyclic shear loads during AFSD.[19] Figure 5a shows a large $Al_{11}Ce_3$ particle that has undergone shear-assisted cracking due to cyclic loading occurring during AFSD, similar to friction stir processing.[29] These cracks grow in size and eventually the particles break down into smaller intermetallics and flow into the matrix under the shearing action of the tool, as shown in Fig. 5b. Figure 5c shows a higher-magnification SEM micrograph where a cluster of fine fragmented intermetallics are dispersed from the parent particle into the matrix. Dissolution of thermally stable precipitates is possible at elevated temperatures when combined with severe plastic deformation.[29] There is no possibility of shear-assisted dissolution in Al-8Ce-10Mg due to the near-zero solubility of Ce in Al; however, there is potential for particle breakdown during AFSD. The study by Palanivel et al.[29] also showed thermally stable intermetallics dissolved on the advancing side and fragmented on the retreating side during friction stir processing. Fragmentation of the intermetallics occurs when the stress on the particle exceeds its critical fracture stress. A similar approach can also be applied to AFSD sample. Since advancing and retreating sides alter during each layer of deposition, AFSD can be an effective processing route to fragment the particles and distribute them uniformly throughout the matrix.

Nanoindentation is an effective tool to characterize and delineate small-scale strain/stress gradients.[30] Nanoindentation was performed on the $Al_{11}Ce_3$ precipitates in BM and AFSD conditions to obtain nanomechanical insights into the shear-assisted fragmentation mechanism activated by variation in the local stress/strain gradient. A compilation of nanoindentation force–displacement (P–h) curves corresponding to both conditions is presented in Fig. 6a. The nanoindented regions

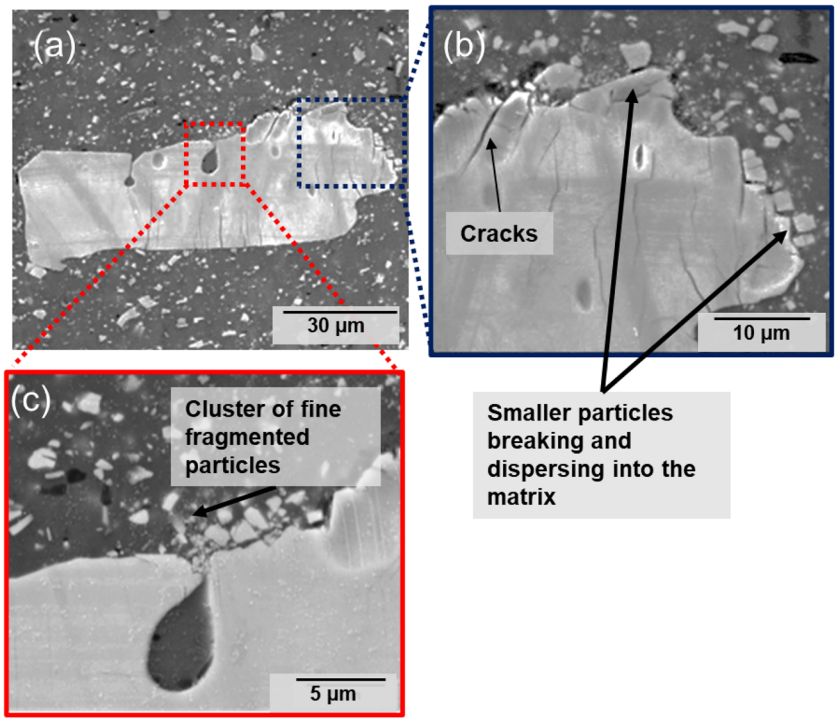

Fig. 5. Complex dynamics of AFSD influence $Al_{11}Ce_3$ particle fragmentation: (a) low magnification of a large particle undergoing shear during AFSD, (b) and (c) high-magnification images showing cracking and breakdown of fine intermetallics away from the parent particle.

were captured using SEM and the micrographs are shown in Fig. 6b. Compared to the $Al_{11}Ce_3$ intermetallic in the BM, AFSD leads to a significant increase in hardness, from 7.0 ± 2.1 GPa to 8.3 ± 1.4 GPa. Also, based on slope of the unloading section of the *P–h* curves, moderately higher stiffness is observed for $Al_{11}Ce_3$ particles in the AFSD processed sample. Exposure to complex stress states in the AFSD process results in large-scale elasto-plastic loading of both matrix and particle. However, the elastic stresses in the matrix and particle varies due to inherent differences in their elastic modulus. The mismatch is accommodated in the form of geometrically necessary dislocation at the particle–matrix interface. Additionally, during frictional heating and subsequent cooling, mismatches in the CTE of the matrix and particle contribute to strain localization at the particle–matrix interface. The strain localization is non-uniform and varies directionally due to the complex motion of the material under the tool. Nanoindentation performed near the interface region (marked by the red circle in Fig. 6b) demonstrates significantly lower hardness (5.58 GPa) than the middle region of the $Al_{11}Ce_3$ particle (8.29 GPa). The *P–h* curve corresponding to this region shows a distinct pop-in event, which is most likely contributed by a cracking event under the tip.[30,31] Note that, in both cases, the indenter interacts with a homogenous $Al_{11}Ce_3$ volume, and that the only variation lies in spatial proximity with respect to the shear localized/fragmented boundary. This suggests particle cracking under the intense shear stress imparted during nanoindentation.

Effect of Thermally Stable Fragmented Particles on Microstructure

The breakdown of particles as demonstrated in the previous section is expected to have a significant influence on the microstructural evolution during AFSD. EBSD analysis rendered a better comprehension of the microstructural change due to AFSD. Figure 7a and b displays inverse pole figure (IPF) micrographs of the BM and AFSD samples, respectively. Note that the unindexed parts of the IPF map correspond to $Al_{11}Ce_3$ intermetallic particles. The base material contains a wide distribution of grain size along with broad particle size distribution. The AFSD sample shows grain refinement due to dynamic recrystallization.[32] Grain size in the BM varied from 1 μm to 11 μm with an average grain size of 8 ± 3.7 μm. The AFSD sample had an average grain size of 4.5 ± 1.5 μm. The presence of fine, thermodynamically stable intermetallic particles pin the newly-formed grain boundary during the dynamic deformation process and thereby prevents further growth. Such thermally stable particles effectively inhibit grain growth and initiate recrystallization.[33] XRD and DSC experiments were performed to obtain further insights into the microstructure and to comprehend thermal stability of the material on exposure to elevated temperatures.

BM and AFSD samples were subjected to DSC to analyze the microstructural stability on exposure to elevated temperatures. The DSC plots are shown in Fig. 8a. Exothermic peaks determine the formation of a phase or crystallization phenomenon, whereas an endothermic peak signifies dissolution of the precipitate or melting. The DSC plots show an endothermic peak at lower temperatures ranging between 50°C and 200°C. These peaks denote the dissolution of Mg in the matrix.[34] Figure 8b shows the EDS of the as-extruded BM, denoting the elemental composition. From the EDS maps, the matrix is observed to be rich in Al and Mg. Ce-rich particles confirm the presence of the $Al_{11}Ce_3$ intermetallic. The magnified image shows Mg-rich clusters in the BM that are undissolved in the Al matrix. Mg-rich and Al-Mg intermetallic were previously observed with the addition of a higher volume fraction of Mg to Al during casting.[35] The Mg segregation is contributed by the high solute partitioning coefficient of Mg in Al at elevated temperatures and the slow cooling rates during casting.[36] Note that the larger peak of the BM sample compared to AFSD sample signifies that a large part of the Mg present in the BM dissolved during AFSD due to intense shear deformation and high-temperature exposure.

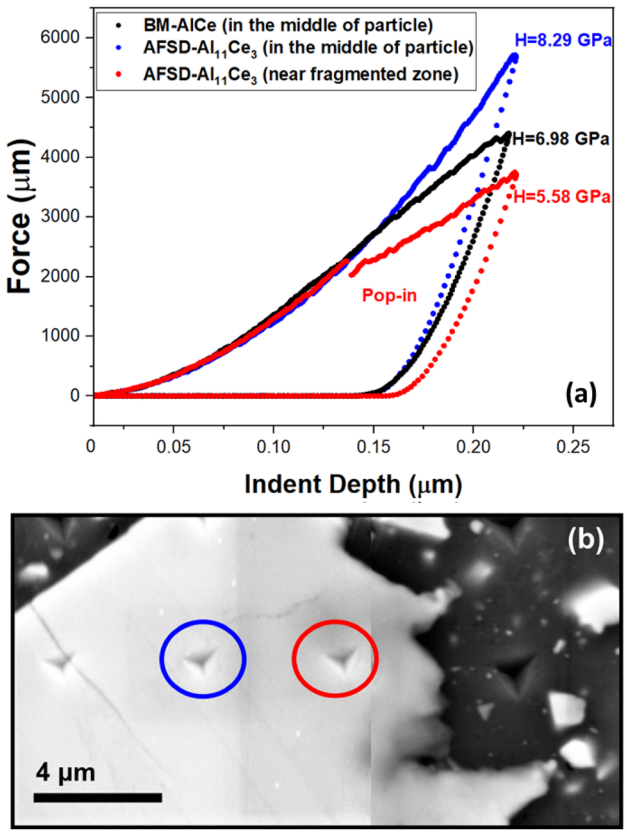

Fig. 6. Effect of stress gradient in AFSD on $Al_{11}Ce_3$ particle investigated by nanoindentation: (a) *P–h* curves captured from distinct locations, and (b) SEM micrographs of the AFSD sample showing indent in the middle and near fragmented zone of the $Al_{11}Ce_3$ particle.

That no other major peaks were analyzed is symbolic of the stability of the second phase ($Al_{11}Ce_3$) on exposure to higher temperatures. The step diagram (Fig. 8c) shows the stability of $Al_{11}Ce_3$ up to 580°C in the equilibrium condition. Although severe plastic deformation processes can accelerate the dissociation kinetics of second phases, the absence of any endothermic/exothermic DSC peaks in the AFSD sample indicates the stability of the $Al_{11}Ce_3$ phase despite severe plastic deformation. Furthermore, the thermally stable fine intermetallics pin the grain boundaries and thereby retard grain growth on exposure to elevated temperatures. Limited Ce solubility in the Al matrix coupled with low Ce diffusion coefficients prevents Ostwald ripening, thereby further enhancing the resistance to grain growth by the $Al_{11}Ce_3$ particles.[17] High thermodynamic stability of $Al_{11}Ce_3$ intermetallic provides ageless behavior upon exposure to higher temperatures.[37] The presence of Mg does not affect the phase constitution of Al-Ce; instead, it reinforces the matrix phase with Al-Mg intermetallic precipitates and metastable pools/clusters that impart improved mechanical properties.[38] Such particle stability empowers the material for

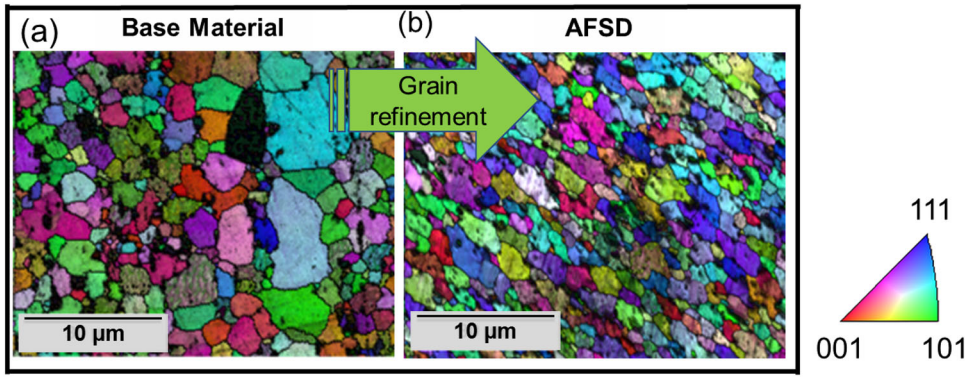

Fig. 7. EBSD IPF map showing grain structure of (a) BM, and (b) AFSD.

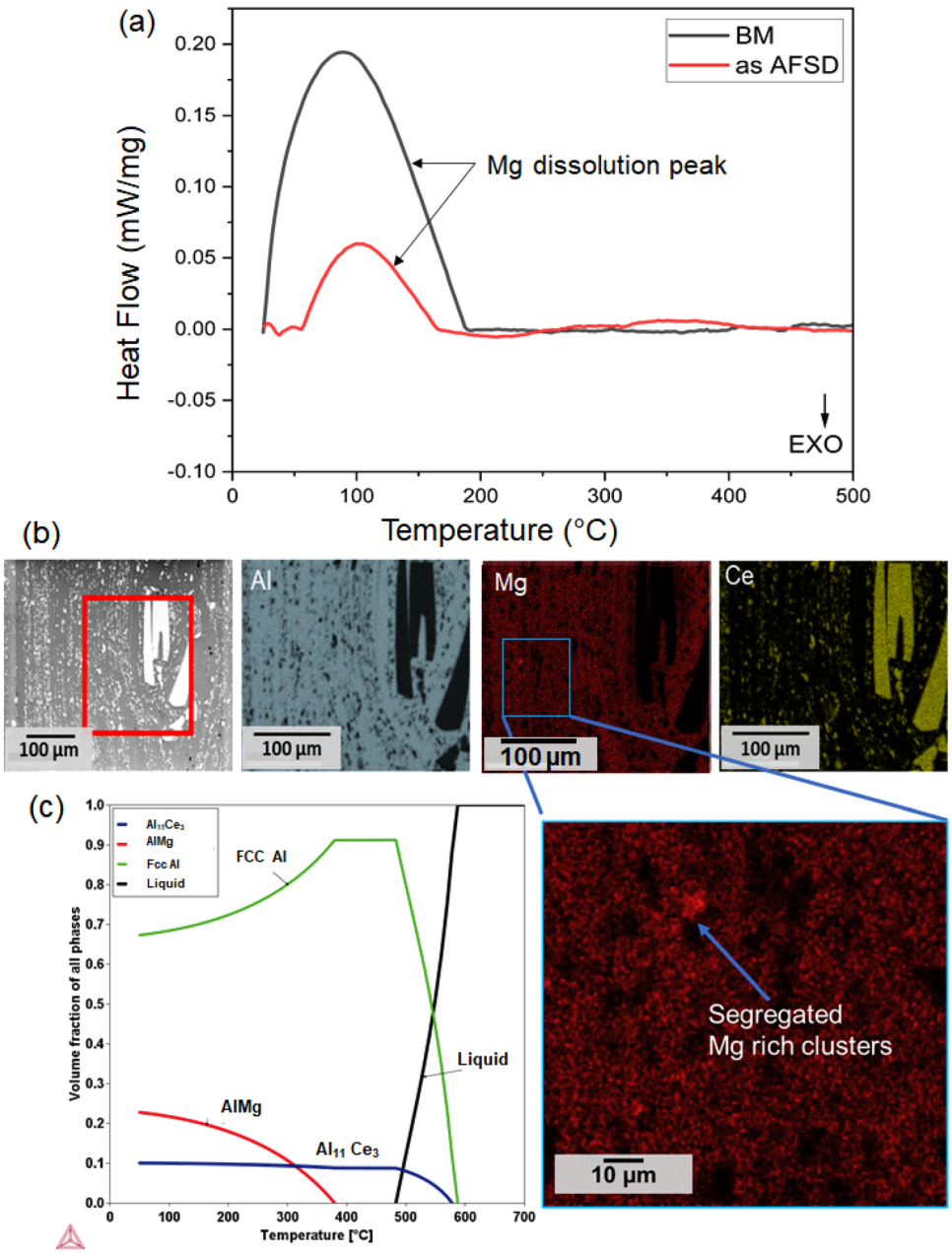

Fig. 8. Thermal stability and phase analysis: (a) DSC curves, (b) EDS maps of the BM, and (c) step diagram representing thermal stability in equilibrium condition.

outstanding mechanical performance at elevated temperatures.

Al-Ce alloys are novel due to the presence of thermally stable intermetallics that yield a stable and temperature-independent microstructure to the alloy.[39] XRD was performed on the BM and AFSD samples to investigate alloy stability. The X-ray diffractogram is shown in Fig. 9. The two phases present in the material have been indexed as Al with dissolved Mg as the matrix, and the $Al_{11}Ce_3$ binary intermetallic. The XRD peaks for BM and AFSD being located at identical diffraction angles confirm no change in the alloy chemistry. By applying Williamson–Hall linear fitting (Eq. 4), the microstrain (ε) and domain size (D) corresponding to the Al matrix in both BM and AFSD conditions were determined:

$$B\cos\theta = \frac{\lambda K}{D} + 4\varepsilon\sin\theta. \quad (4)$$

where B is the full width at half-maximum measured at peak maxima, θ is the Bragg's angle, K is a material constant whose value is usually taken as 0.9 for fcc materials, and λ is the wavelength of the incident CuKα radiation (i.e., 0.154 nm). Applying the numerical values of ε and D obtained from Eq. 4 and using Burgers vector (b) known for Al

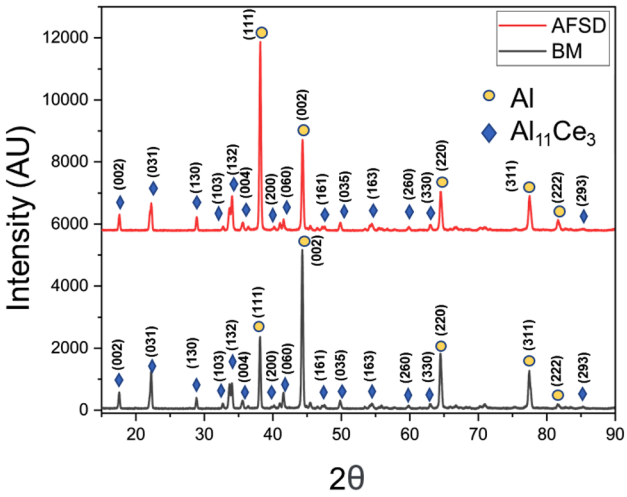

Fig. 9. XRD patterns of BM and AFSD samples.

(0.286 nm), the dislocation density (ρ) was determined using Eq. 5. The values were 0.65 nm^{-2} and 0.43 nm^{-2} for the BM and AFSD samples. The decrease in dislocation density is attributed to dynamic recovery and recrystallization occurring during the AFSD process:

$$\rho = \frac{2\sqrt{3}|\varepsilon|}{Db}. \quad (5)$$

Mechanical Behavior at Different Length Scales

Vickers hardness variation along the height of the sample is plotted in Fig. 10a. The average hardness of BM was 102 HV. Spikes in hardness values ($\sim$ 119 HV) are seen at a couple of points when the indent lies on the large $Al_{11}Ce_3$ particles (inset SEM micrograph of Fig. 10a). The average hardness of AFSD samples is 128 HV and the values drop to 60 HV when the indentation location is on Al 6061 substrate. The relative flatness of the microhardness plot across the build height is indicative of homogeneity in grain size, particle size, and process-induced strain hardening throughout the build. This observation is remarkably different for trends noted in heat-treatable Al alloys, where a progressive drop in hardness can be observed from top to bottom of the deposit. The hardness drop has been attributed to a gradual loss of precipitate strengthening, dislocation annihilation, and grain growth. These phenomena are more prevalent in the bottom layers due to prolonged thermal exposure during the reheat cycles.[7]

Mini-tensile tests were performed to obtain further insights on the mechanical behavior. Figure 10b shows the engineering stress–strain plots for BM and AFSD samples. The BM showed a yield strength (YS) of 192.4 MPa and an ultimate tensile strength (UTS) of 298.7 MPa, at RT. The AFSD material showed a YS of 235.6 MPa and an UTS of 404.6 MPa. The ductility of the AFSD sample at RT was enhanced to 22.5% compared to 8.0% for the BM. The AFSD shows a 22% increase in YS, a 35.5% increase in UTS, and an increase of 181% plastic strain compared to the BM. Serrated plastic flow behavior in the tensile curves is due to the solute drag effect.[40] This effect is commonly observed in Al alloys containing Mg in the solid solution.[41] Mg is an effective solute for pinning of dislocations leading to serrated behavior in Al alloys.

Tensile fracture surfaces for the BM and AFSD at RT were captured by SEM, and their morphology is shown in Fig. 10c and d, respectively. The fracture surface shows a typical transgranular ductile mode of fracture indicated by dimples. The size of dimples in the BM is larger compared to the AFSD sample due to the presence of refined grains. The size of the intermetallic particles also varied in the fractographs. The BM showed larger chunks of clustered particles, which create more crack nucleation sites and, hence, reduce their ductility. The AFSD sample showed fine evenly dispersed particles due to fragmentation. The dimples contained fragmented $Al_{11}Ce_3$ intermetallic, which implies good adhesion between the particles and the matrix. Furthermore, there was no visible evidence of $Al_{11}Ce_3$ particle pull-out after tensile testing of the alloy, which has been commonly observed in metal matrix composites, indicating poor reinforcement–matrix adhesion. The faceted surface of the intermetallic particles revealed that they undergo fracture during tensile loading. Hence, the particles contributed to composite strengthening in the alloy.

Macro-/microscale mechanical tests (tensile and Vickers microhardness) cannot delineate the nanomechanical response due to ultrafine particle refinement. Hence, nanoindentation plots that correspond to regions with very fine $Al_{11}Ce_3$ particles in the AFSD sample were analyzed and compared with a region largely free from $Al_{11}Ce_3$ particles in the BM sample (i.e., representative of the Al-Mg matrix). High-magnification SEM was used to identify these critical indents. In Fig. 11a, hardness plots (H–h) corresponding to the region with ultrafine particles (black) reveal a deviation from the region devoid of particles (red). The hardness response observed after contact is due to the introduction of geometrically necessary dislocations to accommodate the nanoindentation tip. This phenomenon is termed the indentation size effect (ISE). Following the ISE region, the hardness of both samples is similar, as, in both cases, the interaction is limited to the Al-Mg matrix. Following this, a sudden rise in hardness was observed for the AFSD sample with ultrafine $Al_{11}Ce_3$ particle distribution, which plateaus up to a certain indentation depth, and gradually decreases further until the maximum penetration depth. These change in trends is denoted by the four stages of material–indenter interaction illustrated in Fig. 11a and b. The rise in hardness is attributed to the activation of various

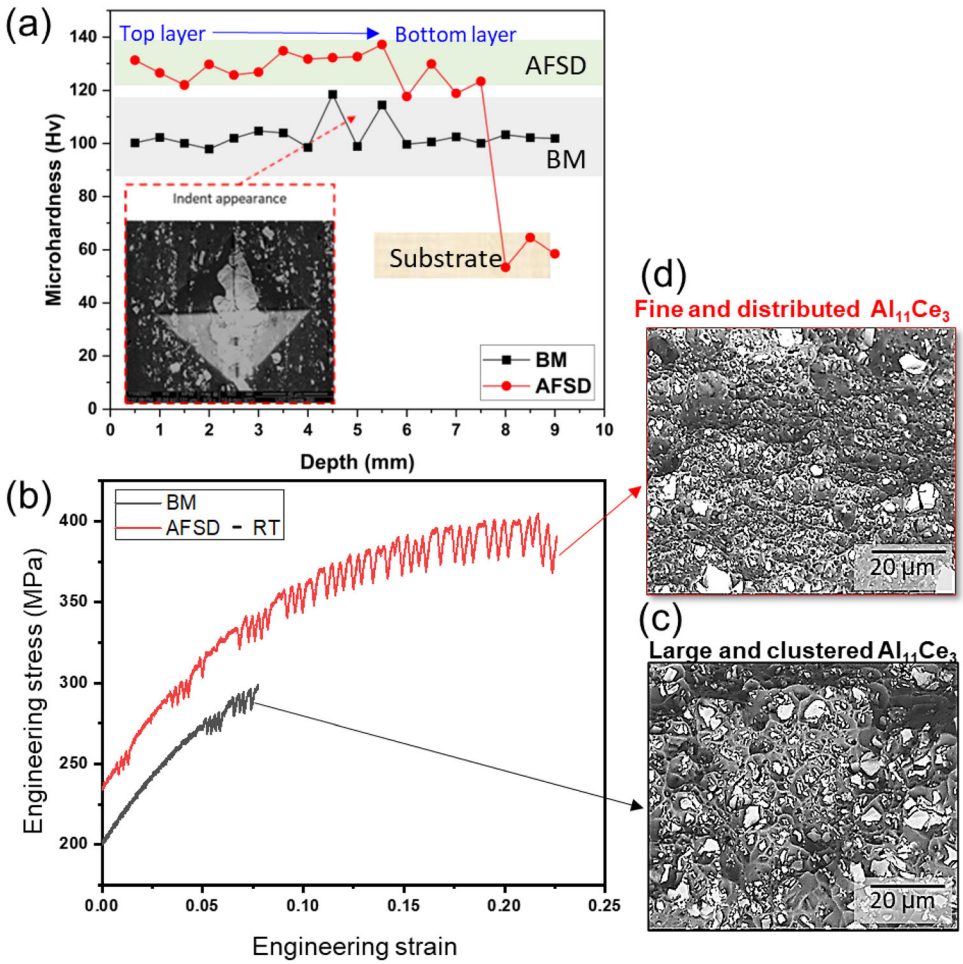

Fig. 10. Investigation of mechanical properties: (a) Vickers microhardness plots, inset the micrograph of the indent on a large chunk of the $Al_{11}Ce_3$ intermetallic, and (b) engineering stress–strain graph at RT; SEM micrographs of fractured surfaces of (c) BM and (d) AFSD tested at RT.

strengthening mechanisms under the tip. Orowan loops may form under the tip around particles with ultrafine size and narrow inter-particle spacing.[42] Larger particles contribute to strengthening through load transfer due to higher stiffness. As the indentation progresses, particle crowding phenomena may occur due to the large modulus and hardness mismatch between the Al-Mg matrix and the $Al_{11}Ce_3$ particles.[43] The crowded particles eventually provide high rigidity and may crack under intense hydrostatic pressure at elevated indentation depth. This cracking is marked by a definitive pop-in in the penultimate loading stage in the corresponding P–h curve (Fig. 11c). The reduction in hardness may be a response to the progressive crack formation and branching mechanism under the tip in the $Al_{11}Ce_3$ particles.

Strengthening Mechanisms and Elevated Temperature Performance

An increase in mechanical properties across all length scales is evident from detailed mechanical characterization. Such enhanced performance in the as-deposited state can be attributed to multiple strengthening mechanisms being activated in the system.

Grain-boundary strengthening, also called the Hall–Petch strengthening effect, is achieved by decreasing the average grain size to a certain limit where dislocation slip is active in the material. Refinement of grains leads to an increase in the grain boundary area. Grain boundaries act as pinning points and obstruct dislocation motion. AFSD leads to the development of refined equiaxed grains due to dynamic recrystallization.[44] EBSD analysis proved that the grain refinement led to an approximately 50% reduction in grain size. The Hall–Petch strengthening contribution to the alloy can be calculated by:

$$\sigma_{HP} = \sigma_0 + Kd^{-0.5}, \quad (6)$$

where σ_0 = 9.8 MPa is the frictional stress for Al, K = 90 MPa $\sqrt{\mu m}$ is the Hall–Petch coefficient, and d is the average grain size.[45,46] Considering the mean grain size (Fig. 7), $\sigma_{hall-petch}$ for BM and AFSD samples are calculated as 41.6 MPa and 52.2 MPa, respectively.

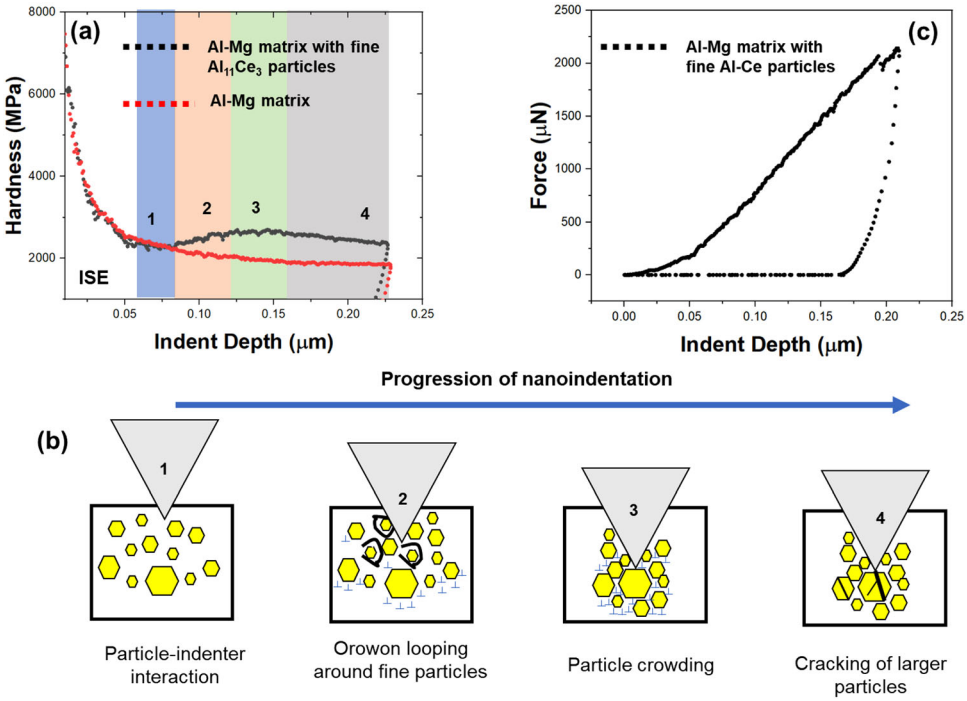

Fig. 11. Nanomechanical properties because of ultrafine $Al_{11}Ce_3$ particles distribution: (a) hardness plots, (b) illustration of material–indenter interaction, and (c) *P–h* curve corresponding to the indentation of an ultrafine particle-rich region in the AFSD sample.

Dislocation strengthening is offered by statistically stored dislocation forest/entanglement. XRD results describe the reduction of dislocation density after AFSD, which is due to dynamic recovery and recrystallization activated during AFSD. The contribution of dislocation strengthening in the alloy can be computed using Taylor's equation:

$$\sigma_D = M\alpha G b\sqrt{\rho_{GND}} \tag{7}$$

where $M = 3$ is the Taylor factor,[47] $\alpha = 0.3$ is a dimensionless interaction constant,[48] $G = 26$ GPa is the shear modulus and $b = 0.286$ nm is the Burgers vector of Al. The dislocation strengthening for BM and AFSD is computed to be 6.69 MPa and 5.46 MPa, respectively.

Solid-solution strengthening occurs when an alloying element forms a solid solution in the base metal. The presence of solute atoms creates a non-uniformity in the crystal and thus causes distortion. The non-uniformity leads to impedance in the dislocation motion through the stress field.[49] Mg has an appreciable amount of solubility in aluminum at elevated temperatures. DSC and EDS maps revealed Mg segregations in the BM which dissolved into the Al matrix during AFSD, due to high-temperature exposure and intense shear deformation. This indicates that solid-solution strengthening may be moderately elevated after AFSD. Ce that has been alloyed beyond the solubility limit forms an intermetallic and does not contribute to solid-solution strengthening. The solute strengthening mechanism can be computed using Fleischer's equation:

$$\sigma_{ss} = \frac{Gc^{\frac{1}{2}}\left(\varepsilon'_G - m\varepsilon_b\right)^{3/2}}{\alpha}, \tag{8}$$

where $c = 8$ wt.% is the concentration of solute atoms, $\varepsilon'_G = -0.155$ is equivalent to $(\varepsilon_G/1 + 0.5\varepsilon_G)$ which is the average modulus mismatch factor, $\varepsilon_b = 0.058$ is the atomic size mismatch factor, and $m = 3$ and $\alpha = 700$ are constants.[50] The solid-solution strengthening in the alloy for both BM and AFSD material is considered to be approximately 20.38 MPa.

Severe plastic deformation techniques can break the particles to micro-/nanoscales.[51] The presence of particles gives a load-bearing effect leading to alloy strengthening. In such cases, strengthening arises due to CTE mismatch between the matrix and the $Al_{11}Ce_3$ particles that leads to the generation of geometrically necessary dislocations, Orowan strengthening, and load-bearing effect. Closely spaced fine-scale hard particles in the matrix obstruct the dislocation motion. This barrier leads to the component of Orowan strengthening in the alloy. Alternatively, in multiphase systems with relatively large-sized particles, strengthening occurs via the load transfer effect.[52] Such a mechanism requires good bonding between the matrix and the particles. The cleavage fracture of the

Table I. Comparison of calculated contribution of strengthening mechanisms to the overall experimental mechanical properties of the Al-Ce-Mg alloy

Strengthening mechanism	Base material (MPa)	AFSD material (MPa)
Hall–Petch strengthening (σ_{HP})	41.61	52.22
Dislocation strengthening (σ_{D})	5.46	6.69
Solid-solution strengthening (σ_{ss})	20.38	20.38
Load-bearing strengthening (σ_{LB})	86.11	99.29
Total theoretical strength calculated ($\sigma_{\text{total calculated}}$)	154.8	177.3
Experimental YS ($\sigma_{\text{experimental}}$)	192.4	235.6

intermetallic shown in the fractographs (Fig. 10c, d) revealed good bonding with the matrix, and the particles contribute to composite strengthening of the alloy. The load transfer strengthening for the alloy can be calculated by Ref. 53:

$$\sigma_{LB} = \left(1 + 0.5V_p\right)\left[\sigma_{ym} + A + B + \frac{AB}{\sigma_{ym}}\right], \quad (9)$$

$$\text{where} \quad A = 1.25G_m b\sqrt{\frac{12\Delta T\Delta\alpha V_p}{bd_p(1-V_p)}} \quad \text{and}$$
$$B = \frac{0.13G_m b}{d_p\left[\left(\frac{1}{2V_p}\right)^{1/3} - 1\right]}\ln\left(\frac{d_p}{2b}\right), \quad (10)$$

σ_{ym} = 34 MPa is the YS of the monolithic matrix, V_p = 22% is the volume fraction of particles and is approximately the same for BM and AFSD, ΔT = 398 K is the difference between the processing and test temperatures, $\Delta\alpha = 13.1 \times 10^{-6}\ K^{-1}$ is the difference in CTE,[54] and d_p is the average particle size and is measured as 5 μm for the BM and 3.5 μm for the AFSD material. Using these, the values of A are 28.6 MPa and 34.26 MPa, and that of B are 5.57 MPa and 7.65 MPa, for the BM and AFSD material, respectively. Thereby, σ_{LB} for the BM and AFSD material is calculated as 80.97 MPa and 92.82 MPa, respectively.

The individual contribution of the strengthening mechanisms is summarized in Table I. The calculated theoretical strength matches closely to the experimental strength of the BM (ΔYS_{BM} = 37.6 MPa). However, for the AFSD material, a larger deviation in YS (ΔYS_{AFSD} = 58.3 MPa) is observed which may be attributed to the strength contributed by an increased fraction of ultra-fine particles.

The aforementioned strengthening mechanisms combine to provide enhanced mechanical properties to the alloy at RT as well as at elevated temperatures. Precipitate-strengthened alloys deteriorate in strength due to the dissolution of the strengthening precipitates on exposure to higher temperatures during friction-stir based processes.[6] However, $Al_{11}Ce_3$ intermetallics are retained, despite exposure to higher processing temperatures, as they are thermally stable to enhance the mechanical properties. Figure 12a shows the mechanical response of AFSDed material at elevated temperatures. The AFSDed alloy shows a YS of 195.8 MPa, a UTS of 248.3 MPa, and a ductility of 23.2% at 150°C. The YS at 150°C is comparable to that of BM with a 200% increase in ductility. At 200°C, the YS is 166.7 MPa, the UTS is 195.6 MPa, and the ductility is 38.5%. At 300°C the YS is 54.9 MPa and the UTS is 77.9 MPa, while total plastic strain is 83.62%. The YS of the material at 350°C reaches very close to the UTS value, with the YS of 24.83 MPa and the UTS 31.9 MPa, while the ductility is almost 135%. The material loses its work-hardening ability as the temperature increases. Figure 12b shows a summary plot comparing the YS, the UTS, and the plastic strain, all of which are listed in Table II.

The serrated behavior of the AFSD at RT is diminished at elevated temperatures. This occurs when the diffusion rate of the solute is comparable to the dislocation velocity.[55] The elevated temperature promotes faster diffusion of the solute from the matrix, which is in a similar order of the dislocation motion. The retention of moderately high tensile strength up to temperature of 200 °C indicates the possible retention of many strengthening mechanisms, e.g., Hall–Petch and the load-bearing effect. These mechanisms are active due to the high thermal stability of the $Al_{11}Ce_3$ particles. The fine particles pin the grain boundaries and retard the grain growth, thereby extending the Hall–Petch strengthening effect at elevated temperatures. Stabilization of the refined grains at high temperatures can be attributed to the Zener pinning effect, which is quantified in terms of the Zener drag force (Fz). Mathematically, Fz imparted by particles is related to ratio between the particle size and the volume fraction of the particles and is expressed as:

$$F_z = K\left(\frac{f\lambda}{r}\right), \quad (11)$$

where λ is the interfacial energy between the grains and the particle boundary, k is the coherency constant, r is the average radius of the particles, and f is the particle volume fraction.

CONCLUSION

This study highlights the synergistic process-specific alloy design to maximize performance. The thermally stable Al-8Ce-10Mg alloy was successfully fabricated using additive friction stir deposition (AFSD) with the following important findings:

- AFSD led to effective grain refinement, particle fragmentation, and homogeneous distribution of the fragmented thermally stable intermetallic particles.
- The as-deposited alloy exhibited superior mechanical properties compared to the base material. Hall–Petch strengthening imparted by refined grains and the load-bearing effect due to fragmented particles were the major strength contributors.
- The AFSD material displayed enhanced mechanical properties at elevated temperatures. Fragmentation of thermally stable particles effectively pins the grain growth to impart an elevated temperature performance.

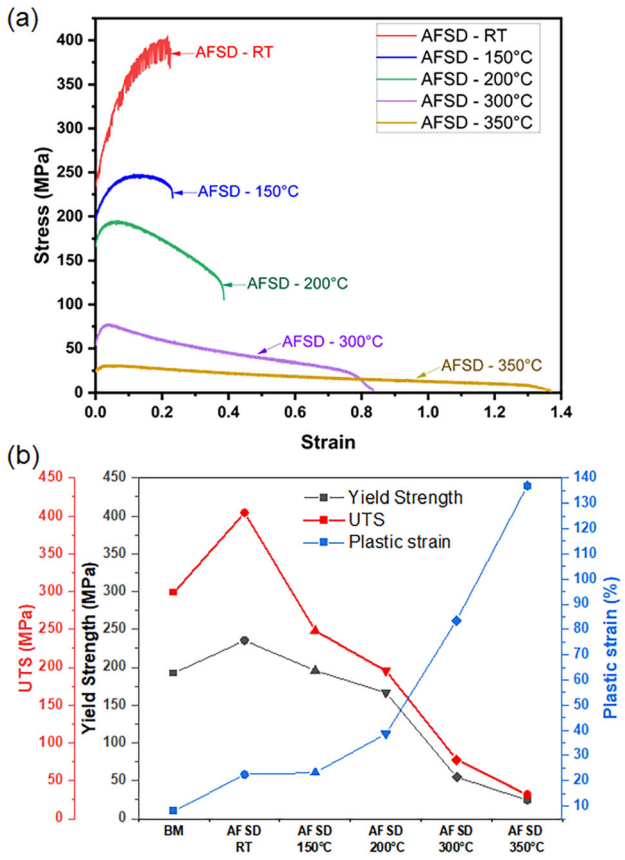

Fig. 12. (a) Engineering stress–strain graph of AFSD at elevated temperatures, and (b) summary plot comparing the tensile properties of BM at RT and of AFSD at varying elevated temperatures.

ACKNOWLEDGEMENTS

The authors are thankful to grants from the Advanced Manufacturing Office (DE-EE0010220). Authors acknowledge Materials Research Facility (MRF) and Center for Agile and Adaptive Additive Manufacturing (CAAAM) at the University of North Texas for access to microscopy and AFSD facilities.

CONFLICT OF INTEREST

The authors declare no conflict of interest.

REFERENCES

1. A. B. Badiru, V. V. Valencia, and D. Liu, in *CRC Press*, edited by A. B. Badiru, V. V. Valencia, and D. Liu, 1st Edition (Taylor and Francis, 2017), p. 938.
2. W.E. King, A.T. Anderson, R.M. Ferencz, N.E. Hodge, C. Kamath, S.A. Khairallah, and A.M. Rubenchik, *Appl. Phys. Rev.* 2, 041304 (2015).
3. H.Z. Yu and R.S. Mishra, *Mater. Res. Lett.* 9, 71 (2021).
4. R.S. Mishra, R.S. Haridas, and P. Agrawal, *Sci. Technol. Weld. Join.* 27, 141 (2022).
5. P. Agrawal, R.S. Haridas, P. Agrawal, and R.S. Mishra, *Addit. Manuf.* 60, 103282 (2022).
6. A. Gumaste, R.S. Haridas, S. Gupta, S. Gaddam, K. Kandasamy, B.A. McWilliams, K.C. Cho, and R.S. Mishra, *J. Mater. Process. Technol.* 316, 117952 (2023).
7. H. Ghadimi, H. Ding, S. Emanet, M. Talachian, C. Cox, M. Eller, and S. Guo, *Materials* 16, 1278 (2023).
8. D.Z. Avery, C.E. Cleek, B.J. Phillips, M.Y. Rekha, R.P. Kinser, H.M. Rao, L.N. Brewer, and P.G. Allison, *J. Eng. Mater. Technol.* 144, 31003 (2022).
9. A. Raman, *Int. J. Mater. Res.* 68, 163 (1977).
10. A.A. Martin, J.A. Hammons, H.B. Henderson, N.P. Calta, M.H. Nielsen, C.C. Cook, J. Ye, A.A. Maich, N.E. Teslich, T.T. Li, M.J. Thompson, M.F. Besser, M.J. Matthews, R.T. Ott, O. Rios, S.K. McCall, T.M. Willey, and J.R.I. Lee, *Appl. Mater. Today* 22, 100972 (2021).
11. H.W. Gillett and V.H. Schnee, *Ind. Eng. Chem.* 15, 709 (1923).

Table II. Mechanical properties of the BM and AFSD material at varying temperature

Sample	YS (MPa)	UTS (MPa)	Plastic strain (%)
BM—RT	192.4	298.6	8.0
AFSD—RT	235.6	404.6	22.5
AFSD—150°C	195.8	248.2	23.2
AFSD—200°C	166.6	195.6	38.5
AFSD—300°C	54.9	77.9	83.6
AFSD—350°C	24.8	31.9	136.9

12. N.A. Belov, E.A. Naumova, and D.G. Eskin, *Mater. Sci. Eng. A* 271, 134 (1999).
13. N.A. Belov and A.V. Khvan, *Acta Mater.* 55, 5473 (2007).
14. P.T. Summers, Y. Chen, C.M. Rippe, B. Allen, A.P. Mouritz, S.W. Case, and B.Y. Lattimer, *Fire Sci. Rev.* 4, 1 (2015).
15. J. Stroh, D. Sediako, and D. Weiss, *Int. J. Metalcast.* 15, 29 (2021).
16. V. Raghavan, *J. Phase Equilibria. Diffus.* 28, 453 (2007).
17. A. Plotkowski, O. Rios, N. Sridharan, Z. Sims, K. Unocic, R.T. Ott, R.R. Dehoff, and S.S. Babu, *Acta Mater.* 126, 507 (2017).
18. S.S. Joshi, S.M. Patil, S. Mazumder, S. Sharma, D.A. Riley, S. Dowden, R. Banerjee, and N.B. Dahotre, *J. Magnes. Alloys* 10, 2404 (2022).
19. B.J. Phillips, C. Jacob Williamson, R.P. Kinser, J. Brian Jordon, K.J. Doherty, and P.G. Allison, *Materials* 14, 6732 (2021).
20. N. Zhu, D.Z. Avery, B.A. Rutherford, B.J. Phillips, P.G. Allison, J. Brian Jordon, and L.N. Brewer, *Met. Basel* 11, 1 (2021).
21. W.D. Hartley, D. Garcia, J.K. Yoder, E. Poczatek, J.H. Forsmark, S.G. Luckey, D.A. Dillard, and H.Z. Yu, *J. Mater. Process. Technol.* 291, 117045 (2021).
22. L. Peter Martin, A. Luccitti, and M. Walluk, *J. Manuf. Sci. Eng.* 144, 061006 (2022).
23. B.J. Phillips, C.J.T. Mason, S.C. Beck, D.Z. Avery, K.J. Doherty, P.G. Allison, and J.B. Jordon, *J. Mater. Process. Technol.* 295, 117169 (2021).
24. S.C. Beck, B.A. Rutherford, D.Z. Avery, B.J. Phillips, H. Rao, M.Y. Rekha, L.N. Brewer, P.G. Allison, and J.B. Jordon, *Mater. Sci. Eng. A* 819, 141351 (2021).
25. K. Anderson-Wedge, D.Z. Avery, S.R. Daniewicz, J.W. Sowards, P.G. Allison, J.B. Jordon, and R.L. Amaro, *Int. J. Fatigue* 142, 105951 (2021).
26. J.W. Pew, T.W. Nelson, and C.D. Sorensen, *Sci. Technol. Weld. Join.* 12, 341 (2007).
27. W.J. Arbegast and P.J. Hartley, in *Proceedings of the Fifth International Conference on Trends in Welding Research* (1998), p. 541.
28. D. Garcia, W.D. Hartley, H.A. Rauch, R.J. Griffiths, R. Wang, Z.J. Kong, Y. Zhu, and H.Z. Yu, *Addit. Manuf.* 34, 101386 (2020).
29. S. Palanivel, A. Arora, K.J. Doherty, and R.S. Mishra, *Mater. Sci. Eng. A* 678, 308 (2016).
30. D. Mercier, V. Mandrillon, G. Parry, M. Verdier, R. Estevez, Y. Bréchet, and T. Maindron, *Thin Solid Films* 638, 34 (2017).
31. D.F. Bahr, C.L. Woodcock, M. Pang, K.D. Weaver, and N.R. Moody, *Int. J. Fract.* 120, 339 (2003).
32. M.E.J. Perry, R.J. Griffiths, D. Garcia, J.M. Sietins, Y. Zhu, and H.Z. Yu, *Addit. Manuf.* 35, 101293 (2020).
33. D. Buttinelli, F. Felli, C. Lupi, and F. Marani, *Mater. Sci. Forum* 94–96, 771 (1992).
34. M. Madanat, M. Liu, and J. Banhart, *Acta Mater.* 159, 163 (2018).
35. D. Weiss, *Adv. Cast. Technol.* 4, 47 (2018).
36. I. Vušanović, B. Šarler, and M.J.M. Krane, *Mater. Sci. Eng. A* 413–414, 217 (2005).
37. F. Czerwinski, *Mater. Sci. Eng. A* 809, 140973 (2021).
38. Z.C. Sims, D. Weiss, S.K. McCall, M.A. McGuire, R.T. Ott, T. Geer, O. Rios, and P.A.E. Turchi, *Jom* 68, 1940 (2016).
39. F. Czerwinski, *J. Mater. Sci.* 55, 24 (2020).
40. P. Rodriguez, *Bull. Mater. Sci.* 6, 653 (1984).
41. H. Dierke, F. Krawehl, S. Graff, S. Forest, J. Šachl, and H. Neuhäuser, *Comput. Mater. Sci.* 39, 106 (2007).
42. J. Moon, S. Kim, J. Jang, J. Lee, and C. Lee, *Mater. Sci. Eng. A* 487, 552 (2008).
43. A. Dhal, S. Thapliyal, S. Gaddam, P. Agrawal, and R.S. Mishra, *Sci. Rep.* 12, 1 (2022).
44. J.K. Yoder, R.J. Griffiths, and H.Z. Yu, *Mater. Des.* 198, 2020 (2021).
45. N. Kumar, G. Gautam, R.K. Gautam, A. Mohan, and S. Mohan, *J. Eng. Mater. Technol. Trans. ASME* 139, 011002 (2017).
46. S. Thangaraju, M. Heilmaier, B.S. Murty, and S.S. Vadlamani, *Adv. Eng. Mater.* 14, 892 (2012).
47. B. Srinivas, A. Dhal, and S.K. Panigrahi, *Int. J. Plast.* 97, 159 (2017).
48. F.F. Lavrentev, *Mater. Sci. Eng.* 46, 191 (1980).
49. Ø. Ryen, O. Nijs, E. Sjölander, B. Holmedal, H.E. Ekström, and E. Nes, *Metall. Mater. Trans. A Phys. Metall. Mater. Sci.* 37, 1999 (2006).
50. A. Dhal, S.K. Panigrahi, and M.S. Shunmugam, *J. Alloys Compd.* 726, 1205 (2017).
51. M.Y. Murashkin, I. Sabirov, A.E. Medvedev, N.A. Enikeev, W. Lefebvre, R.Z. Valiev, and X. Sauvage, *Mater. Des.* 90, 433 (2016).
52. M.L. Young, R. Rao, J.D. Almer, D.R. Haeffner, J.A. Lewis, and D.C. Dunand, *Acta Mater.* 57, 2362 (2009).
53. Z. Zhang and D.L. Chen, *Scr. Mater.* 54, 1321 (2006).
54. T. Wu and D.C. Dunand, *Intermetallics (Barking)* 148, 107636 (2022).
55. R.A. Michi, A. Plotkowski, A. Shyam, R.R. Dehoff, and S.S. Babu, *Int. Mater. Rev.* 67, 298 (2021).